Hindawi
Adsorption Science & Technology
Volume 2022, Article ID 9759759, 10 pages
https://doi.org/10.1155/2022/9759759

Research Article

Adsorption Characteristics of Antibiotic Meropenem on Magnetic $CoFe_2O_4$@Au Nanoparticles

Thi Ngoc Mai Pham,[1] **Thi Hieu Hoang**,[1] **Thu Phuong Nguyen**,[1] **Quang Khanh Nguyen**,[1,2] **Bach Pham**,[1] **Quoc Anh Hoang**,[1] **Tien Duc Pham**,[1] **Thi Anh Huong Nguyen**,[1] **Anh Tuan Le**,[3,4] **and Duc Thang Pham**[3,4]

[1]*Faculty of Chemistry, University of Science, Vietnam National University, Hanoi, 19 Le Thanh Tong, Hoan Kiem, Hanoi 10000, Vietnam*
[2]*Department of Chemistry, College of Natural Sciences, Hanyang University, Seoul 04763, Republic of Korea*
[3]*Phenikaa University Nano Institute, Phenikaa University, Yen Nghia, Ha Dong, Hanoi 12116, Vietnam*
[4]*Faculty of Materials Science and Engineering, Phenikaa University, Yen Nghia, Ha Dong, Hanoi 12116, Vietnam*

Correspondence should be addressed to Thi Ngoc Mai Pham; phamthingocmai@hus.edu.vn
and Duc Thang Pham; thang.phamduc@phenikaa-uni.edu.vn

Received 18 November 2021; Revised 16 February 2022; Accepted 25 February 2022; Published 30 March 2022

Academic Editor: George Kyzas

Adsorption characteristics of the antibiotic meropenem on a novel magnetic material synthesized by surface coating cobalt iron oxide (CFO) with gold nanoparticles (AuNPs) were systematically investigated. The AuNPs can enhance material adsorption capacity by having high affinity towards the thioether and amine groups in the meropenem structure. Au coverage on the CFO surface decreased the saturation magnetization from 55.8 emu/g to 48.8 emu/g, still allowing synthesized CFO@Au nanomaterials to be magnetically recoverable. The CFO@Au nanomaterials showed enhanced adsorption capacity of 25.5 mg/g at optimum conditions of pH 4.0 adsorption time 120 min, and adsorbent mass 0.05 g. Adsorption equilibrium was in accordance with a monolayer Langmuir isotherm, while the adsorption kinetics followed pseudo-first-order kinetics and intraparticle diffusion models. This work provides a simple method to prepare a magnetic composite material with high adsorption efficiency for meropenem and probably other thioether-containing substances.

1. Introduction

Recently, the combination of metal oxide materials with other functional components or other materials has been extensively studied to produce composite materials with novel properties and unique applicability. Due to the evident advantages of gold nanoparticles (AuNPs), structures of such nanoparticles on core-shell oxides have attracted great attention [1–3]. As an inert metal, Au is extremely valuable as a material coating for magnetic nanoparticle protection, surface modification versatility, strong catalytic capability, and biocompatibility [4–6]. Applications of Au/metal oxide nanocomposites include removal of toxic substances such as Hg, As [7, 8], catalysts for organic compound reduction [9], or CO oxidation [10], analysis of various targets including catechols [11], prostate-specific antigen [10], malachite green [12], and drug carriers for biomedical applications [13, 14]. Among different Au-metal oxide composites, Au/magnetic oxide nanoparticles have frequently been studied since these materials can be used in various fields such as protein purification, biological separation, target delivery, magnetic resonance imaging, therapy, and biosensing. Fe_3O_4 and other iron-containing compounds such as $CoFe_2O_4$ attract much attention thanks to the capacity for surface functionalization as well as its excellent magnetic properties. In addition, it is easy to separate these compounds from solution using an external magnetic field [4, 15–20].

Many studies have been carried out on Fe_3O_4/Au nanocomposites, however, not as many studies have focused on

Au and $CoFe_2O_4$ (CFO) composites. Among magnetic oxides, CFO has advantages of large anisotropy, high coercive field, moderate saturation magnetization, high electromagnetic performance, chemical stability, and good electrical conductivity [21–23]. Studies mostly focus on nanocomposite applications for analytical detection, catalysis, and drug delivery, nevertheless, applications for adsorption of -S- or NH- containing substances, exploiting the strong affinity of gold for sulfur or nitrogen atoms has been scarce.

Meropenem is a pyrrolidinyl dimethyl carbamoyl derivative of thienamycin taken from *Streptomyces cattleya*. It is an injectable antibiotic which currently has the broadest antibacterial spectrum in the carbapenem group [24]. Meropenem is one of the strongest antibiotics to kill harmful microorganisms which are resistant to penicillin and cephalosporin antibiotics. Particularly, the carbapenems have been used as last-resort antibiotics for patients in cases of infectious diseases in intensive care units who are seriously infected with multidrug-resistant biota [25]. So far, the analogs of carbapenems in biological and pharmaceutical matrices have mostly been determined with common separation methods include liquid-liquid extraction and solid-liquid extraction (SPE). However, such methods require several steps and have limited selectivity [26]. Sample treatment coupled with magnetic nanoparticles can provide faster phase separation by applying an external magnetic field and is easily reused. To enhance the separation efficiency, magnetic particles have been surface-functionalized with small organic molecules, polymers, aptamers, antibodies, and metal nanoparticles [27].

The present study is aimed at combining magnetic $CoFe_2O_4$ with AuNPs (CFO@Au) and study the adsorption behavior of meropenem on the composite material, which can later be used for separation and enrichment of meropenem from complicated matrices. Since meropenem molecules contain thioether and amine groups, which strongly bind with the Au surface, adsorption of meropenem on Au-modified CFO particles should be enhanced in comparison with bare CFO material. Studies on the adsorptive removal of meropenem have been reported on adsorbents such as multiwalled carbon nanotubes [28] and rice husk functionalized with Mg/Fe-layered double hydroxides [29]. In these cases, the interaction between meropenem and adsorbents is mainly due to electrostatic, π–π EDA interactions, hydrophobic interactions, and hydrogen bonding to -OH and -NH- group. To the best of our knowledge, there is as yet no research examining adsorption of meropenem on CFO@Au.

The synthesis of Au/metal oxide composites usually involves mixing gold (III) salts with a suspension containing oxide nanoparticles and then reducing gold (III) by a suitable reductant such as sodium citrate [8], extract of the *Allium Sp* plant [9], or tetrakis (hydroxymethyl) phosphonium chloride (THPC) [12]. Aniline and dithiothreitol are used to stabilize AuNPs while substances like (3-aminopropyl) triethoxysilane (APTES) or polyethyleneimine dithiocarbamate (PEI-DTC) are used to functionalize the magnetic oxide surface to form better linkages with Au particles. In our study, CFO was prepared by a hydrothermal method, while AuNPs were prepared and stabilized on the CFO surface by using the conventional sodium citrate or sodium borohydride ($NaBH_4$) reductants and poly (diallyldimethylammonium chloride) PDADMAC polycation as a stabilizer.

2. Materials and Methods

2.1. Reagents and Materials. All chemicals used were analytical grade and were directly used without further purification. Meropenem sodium salt 98% (Figure S1 of Supplementary data) was purchased from Toronto Research Chemicals (Canada). Other reagents were chloroauric acid tetrahydrate ($HAuCl_4.4H_2O$), sodium borohydride ($NaBH_4$), sodium citrate ($Na_3C_6H_5O_7$), sodium hydroxide (NaOH), potassium hydroxide (KOH), hydrochloric acid (HCl), poly (diallyldimethylammonium chloride) (PDADMAC) solution with a molecular weight of 400-500 kg/mol (PDADMAC 20 wt% in H_2O) purchased from Merck (Darmstadt, Germany),Fe $(NO_3)_3.9H_2O$, $Co(NO_3)_2.6H_2O$, (3-aminopropyl) triethoxysilane (APTES) and tris(hydroxymethyl) aminomethane (Tris) buffer purchased from Sigma-Aldrich (USA), and Bondesil-C18, 40 μm, 100 gm purchased from Agilent (USA). Deionized water was used for preparing all solutions.

2.2. Synthesis of Materials

2.2.1. Synthesis of $CoFe_2O_4$ Nanoparticles. Powdered magnetic CFO materials were synthesized by a hydrothermal method. A solution containing $Co(NO_3)_2.6H_2O$ and $Fe(NO_3)_3.9H_2O$ with the Co^{2+}: Fe^{3+} molar ratio of 1 : 2.2 was added to a beaker and adjusted to pH 12 with NaOH. This mixture was then transferred to a thermo-hydrolysis vessel and hydrolyzed at 150°C for 2 h. After being hydrolyzed, the sample was taken out and washed several times with distilled water. The precipitate was collected using magnets and dried at 80°C to produce $CoFe_2O_4$ product as a black powder.

2.2.2. Synthesis of $CoFe_2O_4$@Au Composites

(1) PDADMAC-Stabilized Au. AuNPs were obtained by reducing $HAuCl_4$ with $NaBH_4$ in the presence of PDADMAC as a stabilizer [30]. The freshly prepared dispersion of CFO (50 mg in 50 mL of water) was acidified with 0.1 M of HCl at pH 6.5. While continuous stirring, successively, 152 μL of (3-aminopropyl) triethoxysilane (APTES) and 200 μL of 50 mM $HAuCl_4$ were added. Then, 20 μL of PDADMAC was added to the formed dark brown colloidal nanoparticle solution, and the mixture was stirred for 10 minutes. After that, 2 mL of a freshly prepared solution of $NaBH_4$ (0.05 M) was added dropwise into the formed reddish-brown colloidal nanoparticle solution, and then, the mixture was stirred for 3 h. The obtained substance was collected with magnets, washed with deionized water and alcohol, and then dried at 80°C for 12 h.

(2) Citrate-Stabilized Au. CFO dispersion (0.4 g/100 mL) was mixed with 400 μL of 50 mM $HAuCl_4$. The mixture was heated to boiling under continuous stirring; then, 16 mL of

50 mM sodium citrate was added. The solution was further heated for 20 min to form a reddish-brown colloidal solution. The obtained substance was collected with magnets, washed with deionized water and alcohol, and then was dried at 80°C for 12 h.

2.3. Material Characterization. The crystal structures of CFO and CFO@Au were investigated by X-ray diffraction (XRD) using a D8 Advance X-ray diffractometer (Bruker) with wavelength $Cu_{K\alpha}$ = 1.5406 Å and the 2θ angle range of 20° to 80°. The morphology and particle size distribution of CFO and CFO@Au were analyzed on a JEM 1010 transmission electron microscope (TEM, JEOL) operated at an accelerating voltage of 100 keV. The magnetic hysteresis loops were measured by a vibrating sample magnetometer (VSM, Lakeshore) at room temperature and in an external field up to 5 kG. The infrared spectra were recorded on a Fourier transform infrared spectrometer (FTIR-1S, Shimadzu). The absorption spectra of AuNPs, CFO, and CFO@Au were obtained with a UV-Vis spectrophotometer (UV 1601 PC, Shimadzu) using two 1 cm matched quartz cells at room temperature.

2.4. Meropenem Determination. The concentrations of meropenem before and after adsorption on adsorbent material are determined by capillary electrophoresis with a capacitively coupled contactless conductivity detector (CE-C^4D). The CE instrument was built-in house with a commercial C^4D (ER815, eDAQ, Denistone East, NSW, Australia). Uncoated fused silica capillary (ID of 50 μm and OD of 375 μm), total length 60 cm, effective length 53 cm, was used with buffered eluent composed of 10 mM Tris adjusted to pH 8.0 with acetic acid. Injection was carried out by siphoning at a height of 20 cm for 20 s. Separation voltage was +20 kV [31].

2.5. Batch Adsorption of Meropenem on CFO@Au. To evaluate the adsorption capacity, the adsorbent (0.03-0.1 g) was mixed with 10 mL of meropenem solution (pH from 3.0 to 8.0) having different initial concentrations (30 to 350 mg/L) in 15 mL falcon tubes. These falcon tubes were then shaken in the range of 60 to 300 min. The parameters investigated include solution pH, adsorption time, adsorbent mass, and initial concentration of meropenem.

The concentrations of meropenem after adsorption were determined by using CE-C^4D measurement. The adsorption efficiency ($H_{\%}$) was evaluated by the following equation:

$$H = \frac{C_0 - C}{C_0} \times 100\%. \quad (1)$$

The adsorption capacity q_e (mg/g) of meropenem onto CFO@Au was calculated by the following equation:

$$q_e = \frac{C_0 - C_e}{m} \times V, \quad (2)$$

where C_0 (mg/L) and C_e (mg/L) are the initial concentration and equilibrium concentrations of meropenem, respectively, V (L) is the volume of the solution, and m (g) is the absorbent mass.

Kinetics experiments used initial meropenem concentration of 50 ppm, pH = 4.0 adsorbent mass of 0.05 g, and time ranging 0 to 180 min, while experiments to evaluate adsorption isotherms used initial meropenem concentration varying from 30 to 350 ppm, pH = 4.0, adsorbent mass = 0.05 g, time = 120 min.

2.6. Adsorption Isotherms. Langmuir and Freundlich models were investigated for adsorption isotherms. The Langmuir adsorption isotherm is described by the following equation [32–34]:

$$q_e = \frac{q_m K_L C_e}{1 + K_L C_e}, \quad (3)$$

where q_e and q_m are equilibrium and maximum adsorption capacities (mg/g), respectively, and K_L is the Langmuir adsorption constant (L/mg) which relates to energy of adsorption.

The Freundlich model is as follows [33, 35]:

$$q_e = K_F C^{1/n}, \quad (4)$$

where k_f is Freundlich adsorption capacity (L/g) and n is an indicator for the degree of surface heterogeneity and describes the distribution of the adsorbed molecules on the adsorbent surface. The Freundlich equation is characteristic for a multilayer adsorption isotherm.

2.7. Kinetic Models. To evaluate the rate of the adsorption process, the pseudofirst-order, pseudosecond-order, and intraparticle diffusion models are frequently applied to fit the kinetics data. The correlation coefficient (R^2) is computed to evaluate how successfully the model fits the data and demonstrate the kinetics of adsorption [33].

The pseudofirst-order model is described by equation (5). This model assumes the physical adsorption of one adsorbate molecule onto one active site on the adsorbent surface [33]:

$$q_t = q_e\left(1 - e^{-k_1 t}\right). \quad (5)$$

The pseudosecond-order model follows equation (6). The pseudosecond-order model assumes the adsorption of one adsorbate molecule onto two active sites on the adsorbent surface, preferentially through chemisorption [33]:

$$q_t = \frac{q_e^2 k_2 t}{1 + q_e k_2 t}, \quad (6)$$

where q_e and q_t are equilibrium adsorption capacity (mg/g) and adsorption capacity at different time intervals (mg/g), respectively. t is adsorption time (min), and k_1 and k_2 are pseudofirst-order (1/s) and pseudosecond-order (g/mg.min) rate constants, respectively.

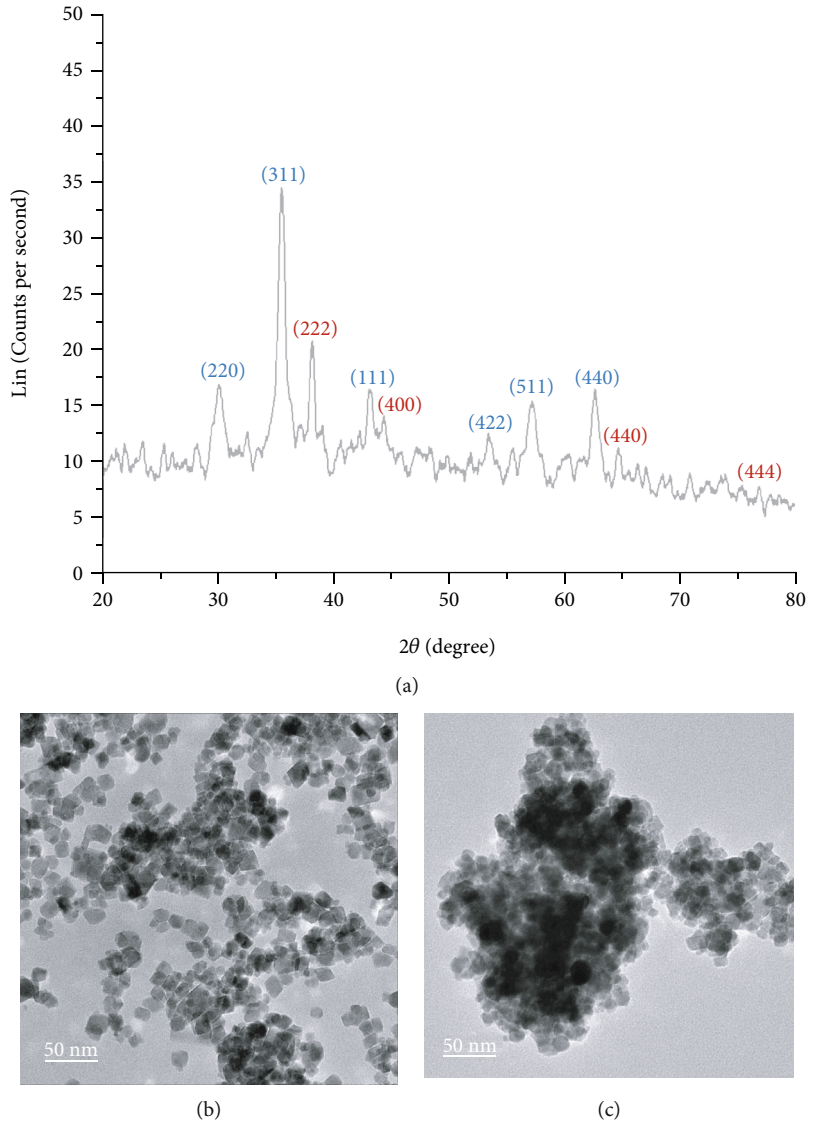

Figure 1: Characterization of CFO@Au: (a) X-ray diffraction pattern of the CFO@Au nanocomposites, (b) TEM images of CFO, and (c) TEM images of CFO@Au particles.

Intraparticle diffusion model provides information about the diffusion of adsorbate onto the adsorbent material and whether intraparticle diffusion is the rate-limiting step. Equation (7) describes the intraparticle diffusion model:

$$q_t = k_d t^{1/2}, \tag{7}$$

where k_d is the intraparticle diffusion rate constant ($1/\text{min}^{1/2}$).

3. Results and Discussion

3.1. Comparison of Meropenem Adsorptivity between CFO@Au-Citrate, CFO@Au-PDADMAC, CFO, and C18 Materials. The adsorption efficiencies of meropenem on CFO@Au composites, prepared by 2 methods, stabilized with citrate and stabilized with PDADMAC, were compared with bare CFO and conventional adsorption material C18 (10 mL of 50 ppm meropenem, pH 4.0; contact time 120 min, adsorbent mass 0.10 g) as presented in Figure S2. Among the 4 materials, C18 provides the lowest adsorption efficiency of 24%, followed by CFO (62%), then CFO@Au-PDADMAC (72%), and the highest efficiency was obtained for CFO@Au-citrate (94%). The modification of CFO by AuNPs enhanced the adsorption efficiency of meropenem through affinity interaction between AuNPs on the surface with thioether and amine groups in the meropenem molecular structure.

The CFO and Au composites synthesized by 2 routes demonstrate not only different adsorption efficiencies but also different pH-dependent adsorption behaviors. For CFO@Au-PDADMAC, when the solution pH was varied from 3.0 to 8.0, the adsorption capacity changed insignificantly and had a maximum at pH 6.0. According to our previous research on the PDADMAC-Au system [30], the interaction between the analyte and PDADMAC is mainly hydrophobic interaction. Meropenem has isoelectric point

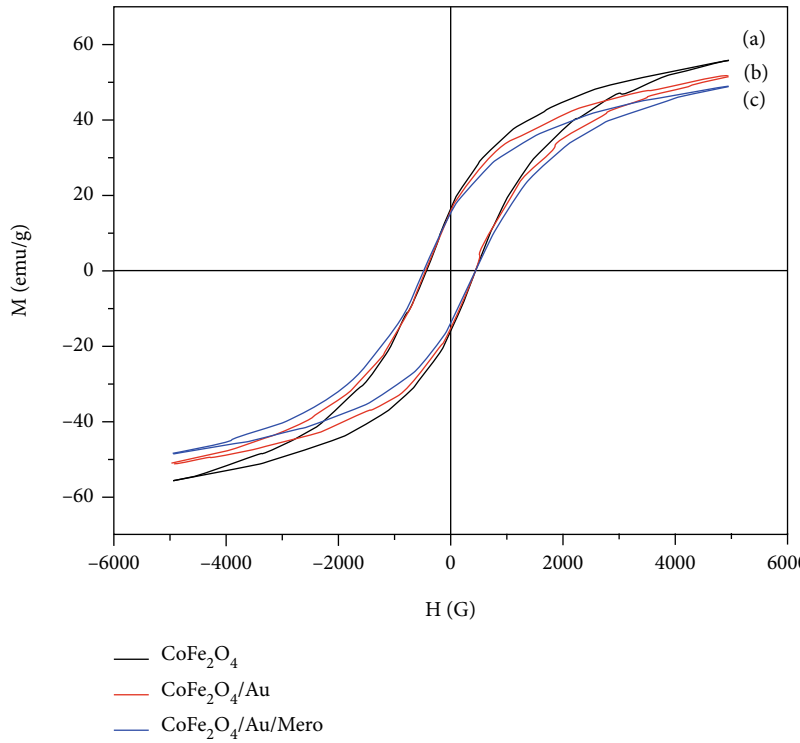

Figure 2: Hysteresis loops of (a) CFO, (b) CFO@Au, and (c) CFO@Au-meropenem.

pI~6.0, meaning that at pH 6.0, it is charge neutral. Thus, meropenem can be adsorbed and distributed very well on the hydrophobic surface of CFO@Au-PDADMAC. The maximum adsorption at pH 6.0 suggests the dominant contribution of hydrophobic interaction between meropenem and PDADMAC capped-AuNPs over the electrostatic interaction.

Meanwhile, for CFO@Au-citrate, the maximum adsorption capacity was obtained at pH 4.0 (94%). This is explained by the dominant electrostatic interaction between citrate-AuNPs and meropenem which vary with pH. Citrate-AuNPs are negatively charged at pH > pK = 3.1 of citric acid. For meropenem, at low pH, meropenem is positively charged and hence is well kept on the negatively charged surface of citrate-AuNPs. At higher pH, the positive charge is reduced; hence, the electrostatic attraction decreases, leading to decreased adsorption efficiency. Since the CFO@Au-citrate composite provides higher adsorption efficiencies than the CFO@Au-PDADMAC, in succeeding parts, we will focus our investigation only on the CFO@Au-citrate system, which is denoted simply as CFO@Au.

3.2. Characterization of CFO@Au. The XRD pattern of the CFO@Au sample is shown in Figure 1(a). Beside the diffraction peaks at 30.1, 35.4, 43.3, 53.6, 57.5, and 63.0°, corresponding to (220), (311), (111), (422), (511), and (440) planes of cubic spinel CFO, there are additional sharp peaks at 38.5, 44.0, 64.0, and 78.0° assigned to (222), (400), (440), and (444) planes of the face-centered cubic Au lattice [36, 37]. This result indicated that the composite of CFO@Au has been successfully synthesized, and both phases are in well-developed crystalline structures.

3.2.1. Surface Morphology. The TEM images of the CFO material (Figure 1(b)) and the CFO@Au composite (Figure 1(c)) reveal that CFO particles have cubic or rectangular shapes with homogenous sizes from 10-20 nm. After coating with Au, the particles remain the same size but tend to form clusters, covered by additional small and round particles, which may correspond to the morphology of single sphere AuNPs prepared by the citrate method [38, 39].

3.2.2. Infrared Spectra. Comparison of FT-IR spectra of CFO@Au (Figure S3a) and CFO@Au-meropenem (Figure S3b) reveals the appearance of several weak bands at 1800-1600 cm^{-1}, typical for valence vibration of the C=O group (1620 cm^{-1}, 1744 cm^{-1}) in spectra of CFO@Au-meropenem [28, 40]. In addition, we have the absorption bands in 1600-1200 cm^{-1} regions belonging to aromatic rings (1566 cm^{-1}, 1520 cm^{-1}, 1398 cm^{-1}, 1291 cm^{-1}); the bands at >3000 cm^{-1} correspond to C-H in aromatic ring (3296 cm^{-1}, 3744 cm^{-1}) and a wide adsorption band in 3400-2400 cm^{-1} to O-H and N-H groups [28, 29]. The existence of organic functional groups belonging to meropenem in FT-IR spectra of CFO@Au-meropenem proves the adsorption of meropenem on the nanocomposite surface.

3.2.3. UV-Vis Spectra. UV-Vis absorption spectra of AuNPs, CFO, and CFO@Au particles dispersed in water were recorded in the wavelength range 400-800 nm (Figure S4).

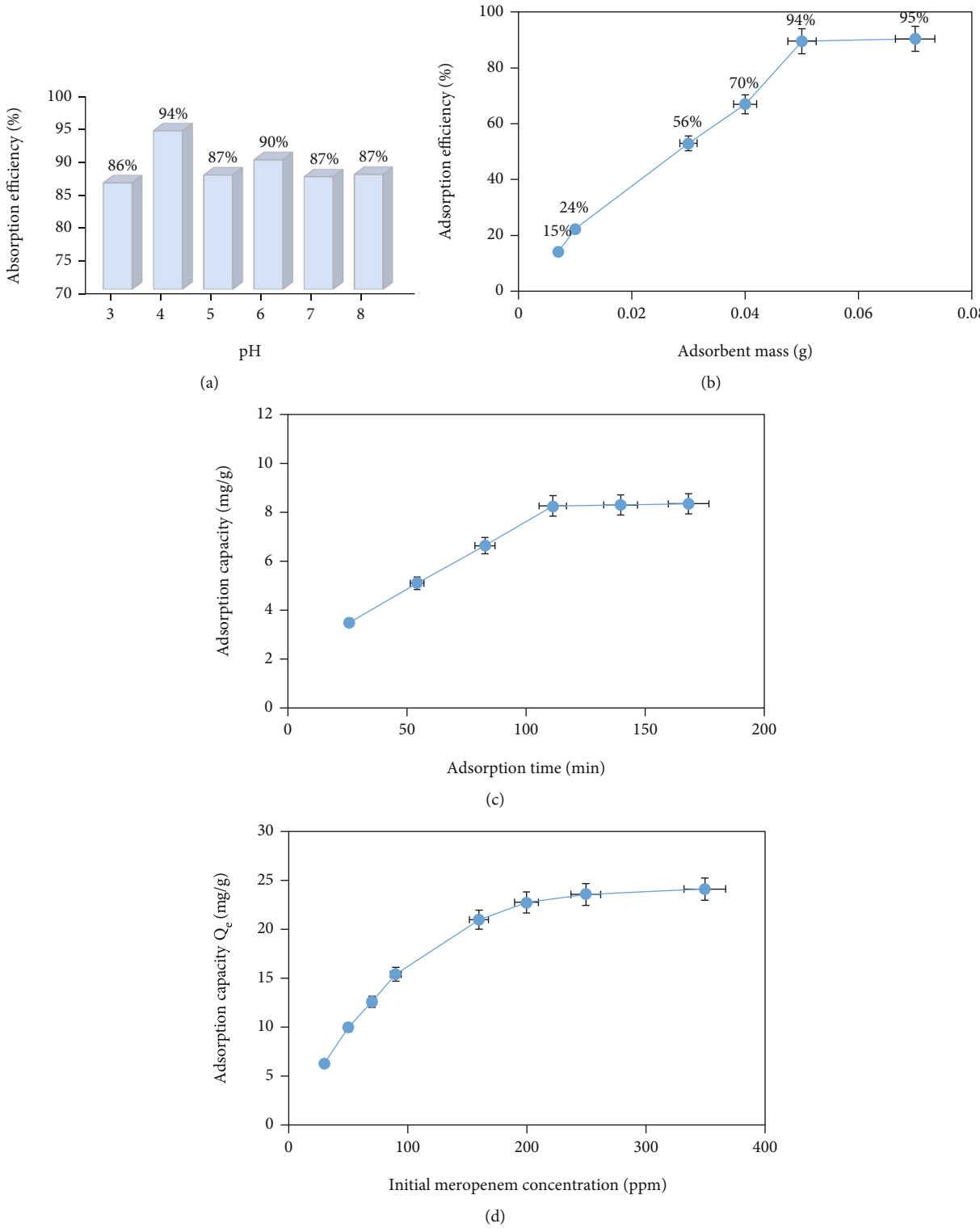

Figure 3: (a) The influence of solution pH on meropenem adsorption efficiency of CFO@Au, (b) the influence of adsorbent mass on meropenem adsorption efficiency, (c) the effect of adsorption time on kinetic adsorption, and (d) the effect of initial meropenem concentration on the adsorption capacity of the material.

CFO particles have no surface plasmon resonance (SPR) absorption in the investigated region, while AuNPs have a plasmon band with maximum absorption at 520 nm, typical for AuNPs having sizes of 10-30 nm [41, 42]. For CFO@Au nanocomposite, a maximum absorption band was detected around 520 nm, but widened and slightly red-shifted. The appearance of the absorption band around 520 nm proved the existence of AuNPs on the surface of

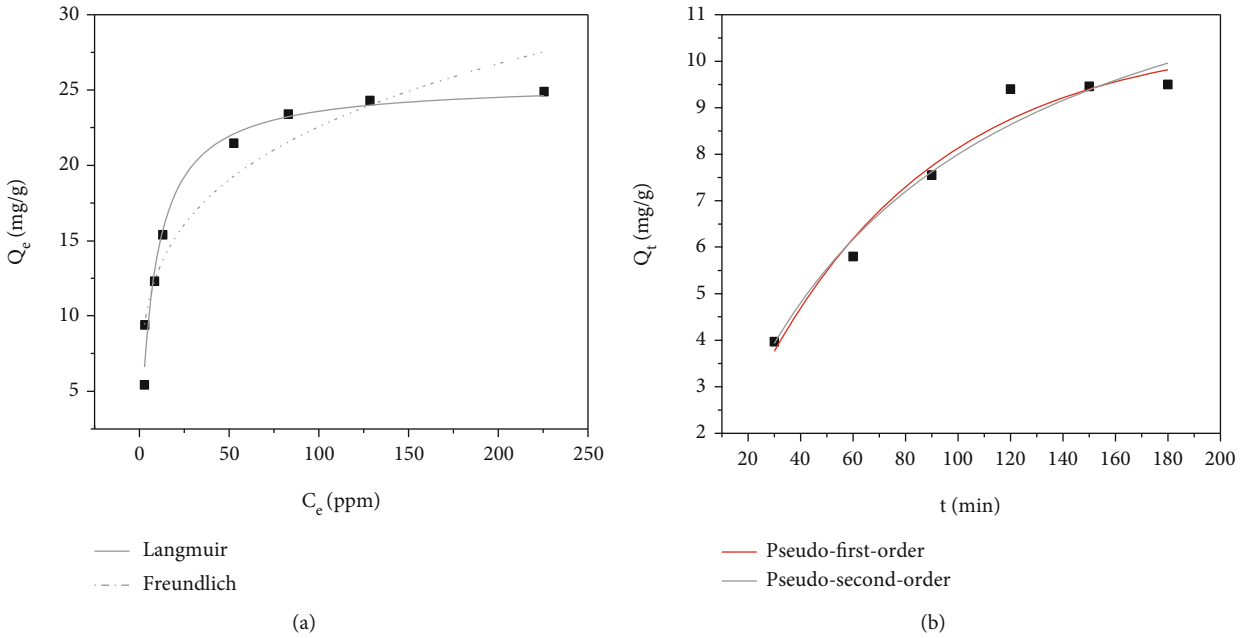

Figure 4: Isotherm and kinetic model fit with experimental data of meropenem adsorption on CFO@Au material. (a) Langmuir and Freundlich isotherm. (b) pseudofirst-order and pseudosecond-order kinetic model.

Table 1: Isotherm parameters of Langmuir and Freundlich models.

Langmuir model		Freundlich model	
Q_{max}	25.5 mg/g	K_F	7.2918
K_L	8.15	$1/n$	0.24513
χ^2	1.509	χ^2	5.705
R^2	0.97693	R^2	0.91281

CFO, as confirmed by XRD measurement. The wavelength shift indicates the change in the dielectric constant of the material, which is inversely proportional to the plasmon vibrational frequency. The widening of the plasmon band is assigned to the decrease of electron exchange of AuNPs adsorbed on the CFO surface [43].

3.2.4. Magnetic Properties. In the CFO@Au composites as well as of CFO@Au-meropenem, CFO plays a role as magnetic support, which helps to easily recover material after using. The magnetic properties of CFO, CFO@Au, and CFO@Au-meropenem were characterized based on magnetic hysteresis loops $M(H)$. The $M(H)$ loops provided in Figure 2 show typical soft magnetic behavior. From these curves, characteristic parameters such as remanent magnetizations and coercivities were derived as $M_r \sim 16$ emu/g and $H_c \sim 430$ G, respectively. The saturation magnetizations M_s differ among these samples as 55.8 emu/g, 51.3 emu/g, and 48.8 emu/g for CFO, CFO@Au, and CFO@Au-meropenem, respectively. The decrease in M_s is due to the coverage of nonmagnetic Au as well as meropenem on magnetic core CFO. Despite this change, the composites CFO@Au and CFO@Au-meropenem still possess good magnetic properties. After meropenem adsorption, CFO@Au powders can be easily separated from the solution after 3 min by using external magnets (Figure S5).

From the above measurements, we confirm that the CFO@Au nanocomposite was successfully fabricated with particle size ranging from 10-20 nm, and that the material has high crystallinity and good magnetic properties. This material was further used to investigate adsorption behavior of meropenem in batch adsorption experiments.

3.3. Adsorption of Meropenem on CFO@Au

3.3.1. Effect of pH. As mentioned in Section 3.1, for CFO@Au-citrate, the highest adsorption efficiency was obtained at pH 4.0 (Figure 3(a)), which is resulted from the strongest attraction force between negatively charged Au-citrate particles and positively charged meropenem at this pH.

3.3.2. Effect of Adsorbent Mass. The adsorbent mass strongly influences the number of adsorption centers, hence, strongly influences the meropenem adsorption capacity. As the adsorbent mass was varied between 0.007 and 0.07 g (see Figure 3(b)), the adsorption efficiency increased and tended to a maximum at 0.05 g. The increase of adsorption capacity with increasing adsorbent mass can be explained by the increase in the number of adsorption centers. However, when the mass of the material is above a certain amount, the adsorption capacity reaches saturation, which corresponds to the saturated adsorption of meropenem. The optimum mass adsorbent was selected as 0.05 g for further studies.

3.3.3. Effect of Adsorption Time. The effect of adsorption time on the meropenem adsorption on CFO@Au was

Table 2: Pseudofirst-order adsorption and pseudosecond-order adsorption rate constants (C_0 = 50 ppm).

Model	Fit equation	R^2	k (g/mg.min)	q_e (exp) (mg/g)	q_e (cal) (mg/g)
Pseudofirst-order adsorption	$q_t = q_e\left(1 - e^{-k_1 t}\right)$	0.97178	0.01466	9.5	10.572
Pseudosecond-order adsorption	$q_t = \frac{q_e^2 k_2 t}{1 + q_e k_2 t}$	0.96455	0.000874	9.5	14.365

investigated in the range from 0 to 180 min with an initial meropenem concentration of 50 ppm, pH 4.0, and adsorbent mass of 0.05 g. Figure 3(c) shows that the uptake of meropenem (q_t) (mg/g) increased with increasing adsorption time and remained nearly constant after 120 min. The adsorption is rapid in the initial stages and gradually decreases with the progress of adsorption. All plots are single, smooth, and continuous curves leading to saturation.

3.3.4. Effect of Initial Meropenem Concentration. Initial meropenem concentration in the solution plays an important role as the movement of the constituents in the solution controls mass transfer between the solution and the adsorbent surface. Systematic investigation on the initial meropenem concentration was further carried out in a wide concentration range from 30 to 350 ppm, at pH 4.0, adsorbent mass of 0.05 g, and time of 120 min. As can be seen in Figure 3(d), the equilibrium adsorption capacity of meropenem increases significantly at low initial meropenem concentrations from 30 to 160 ppm, from 5.43 to 21.47 mg/g, then increases more slowly and reaches a maximum of 24.89 mg/g at meropenem concentration of 350 ppm. These data are further used to deduce the adsorption isotherms of meropenem on CFO@Au.

3.4. Study on the Adsorption Isotherms. The nonlinear regression fit of experimental results with Freundlich and Langmuir adsorption isotherm models are given in Figure 4(a). Comparing the fit parameters of the two models (Table 1), the Langmuir model provides a higher correlation coefficient R^2 of 0.97693 and lower χ^2 of 1.50 than the Freundlich model (R^2 of 0.91281 and χ^2 of 5.705), indicating better experimental agreement with the Langmuir rather than the Freundlich model. Hence, we conclude that the isothermal adsorption of meropenem on CFO@Au is by monolayer adsorption rather than multilayer adsorption, and the distribution of active sites on the surface of the adsorbent is uniform. The maximum adsorption capacity calculated from the Langmuir isotherm is rather high as 25.5 (mg/g), which suggests the potential of the composite material for meropenem adsorption in biomedical applications.

3.5. Study on Kinetic Models of Static Kinetic Adsorption. Diffusional mechanisms can be studied using three kinetic models including pseudofirst-order, pseudosecond-order, and intraparticle models. The regression correlation coefficient, R^2, of these models was used to determine the best-fit model.

3.5.1. The Pseudofirst-Order Model and Pseudosecond-Order Model. Fitting lines and correlation parameters are presented in Figure 4(b) and Table 2. Both pseudofirst-order and pseudosecond-order models have high correlation factors R^2 (0.97178 for pseudofirst-order model and 0.96455 for pseudosecond-order model), indicating that both models could be satisfied and both physical diffusion and chemical adsorption via bonding between SH- group and gold surface are responsible for meropenem adsorption on CFO@Au material. Since the q_e value calculated from the fitted pseudofirst-order model (10.572 mg/g) is closer to q_e experimental (9.5 mg/g), the data seem to better follow the pseudofirst-order model. According to this model, the adsorption of meropenem on CFO@Au was assumed to proceed by diffusion through a boundary, and one adsorbate molecule was adsorbed onto one active site on the adsorbent surface [33].

Our observation on the simultaneous occurrence of physical diffusion and chemical adsorption agrees with other authors [28, 29], however, in their studies, the pseudosecond-order model provides a better account of meropenem adsorption on rice husk functionalized with Mg/Fe layered double hydroxides [29] and on multiwalled carbon nanotubes [28].

3.5.2. The Intraparticle Diffusion Model. Because the first two models did not convincingly describe the diffusion of meropenem onto the material surface, the intraparticle diffusion model was then tried as it is a widely used approach for the analysis of adsorption kinetics. This model states that adsorption changes roughly proportionally to $t^{1/2}$ rather than with contact time t. The adsorbate was most probably transported into adsorbent through an intraparticle diffusion process with three steps. The first step is instantaneous adsorption or external surface adsorption. The next step is the fast adsorption stage, where intraparticle or pore diffusion is rate-limiting, followed by the final equilibrium step, where intraparticle diffusion begins to decelerate due to extremely low adsorbate concentrations remaining in the solutions adjacent to the particles [44, 45]. Adsorption data for q_t versus $t^{1/2}$ is shown in three stages in Figure S6.

According to this model, a plot of q_t versus $t^{1/2}$ should be linear if intraparticle diffusion is involved in the adsorption process. The three steps of the adsorption process are shown by the distinct stages in Figure S6. The slope of the graph is steeper at the start, indicating a boundary layer effect. In this stage, meropenem diffuses fast to the sorbent's surface and into the pores thanks to the driving force of electrostatic

attraction between meropenem and CFO@Au and the affinity interaction between meropenem and Au surface. There is also external resistance to mass transfer around the particles [46]. The second region is the gradual adsorption stage, representing micropore diffusion. Intraparticle diffusion is the rate-limiting step in this region. There is also the third stage, as indicated in Figure S6, where intraparticle diffusion began to slow, because the adsorbent was saturated and the concentrations of solutes were low.

4. Conclusions

We have successfully synthesized a magnetic nanocomposite having high adsorptivity (maximum adsorption capacity of 25.5 mg/g) for meropenem, based on magnetic cobalt ferrite (CFO) and gold nanoparticles. Surface modification of CFO by AuNPs significantly enhanced the adsorption capacity efficiency of meropenem in comparison with bare CFO, thanks to affinity interaction between AuNPs on the surface with thioether and amine groups in the molecular structure of meropenem. The optimum conditions for adsorption of meropenem on CFO@Au were found to be pH 4.0, adsorption time 120 minutes, and adsorbent mass 0.05 g. The adsorption isotherm of meropenem CFO@Au follows well the Langmuir model; differences between first and second-order kinetic models are too small to resolve. Despite the presence of nonmagnetic gold particles, the composite still possesses good magnetic properties, which is helpful for quickly collecting material after adsorption. CFO@Au material can be used for the separation and enrichment of meropenem from an aqueous solution and is also a potential candidate for other applications such as biological separation and target drug delivery.

Data Availability

All the data and supporting materials are included within the article.

Conflicts of Interest

All authors declare that there are no conflicts of interest regarding the publication of this paper.

Acknowledgments

The authors would like to thank Professor Alexander Scheeline, University of Illinois at Urbana-Champaign for giving valuable comments and revising English.

Supplementary Materials

Figure S1: chemical structure of meropenem. Figure S2: adsorption efficiencies of meropenem on C18, CFO, CFO@Au-citrate, and CFO@Au-PDADMAC. Figure S3: IR spectra of (a) CFO@Au; (b) CFO@Au@meropenem. Figure S4: UV-vis absorption spectra of (1) CFO, (2) AuNPs, and (3) CFO@Au solution. Figure S5: separation of CFO@Au-meropenem from aqueous solution using a magnetic stirrer. Figure S6: intraparticle diffusion plots for the adsorption of meropenem. *(Supplementary Materials)*

References

[1] L. Wang, H.-Y. Park, S. I. I. Lim et al., "Core@shell nanomaterials: gold-coated magnetic oxide nanoparticles," *Journal of Materials Chemistry*, vol. 18, no. 23, pp. 2629–2635, 2008.

[2] L. Wang, J. Luo, M. M. Maye et al., "Iron oxide–gold core–shell nanoparticles and thin film assembly," *Journal of Materials Chemistry*, vol. 15, no. 18, pp. 1821–1832, 2005.

[3] M. Smith, M. McKeague, and M. C. DeRosa, "Synthesis, transfer, and characterization of core-shell gold-coated magnetic nanoparticles," *MethodsX*, vol. 6, pp. 333–354, 2019.

[4] C. Karami and M. A. Taher, "A catechol biosensor based on immobilizing laccase to Fe_3O_4@Au core-shell nanoparticles," *International Journal of Biological Macromolecules*, vol. 129, pp. 84–90, 2019.

[5] Y. Xing, Y.-Y. Jin, J.-C. Si et al., "Controllable synthesis and characterization of Fe_3O_4/Au composite nanoparticles," *Journal of Magnetism and Magnetic Materials*, vol. 380, pp. 150–156, 2015.

[6] K. C. Grabar, R. G. Freeman, M. B. Hommer, and M. J. Natan, "Preparation and characterization of Au colloid monolayers," *Analytical Chemistry*, vol. 67, no. 4, pp. 735–743, 1995.

[7] S.-I. Lo, P.-C. Chen, C.-C. Huang, and H.-T. Chang, "Gold nanoparticle–aluminum oxide adsorbent for efficient removal of mercury species from natural waters," *Environmental Science and Technology*, vol. 46, no. 5, pp. 2724–2730, 2012.

[8] S. Banerjee, N. P. Kumar, A. Srinivas, and S. Roy, "Core-shell Fe_3O_4@Au nanocomposite as dual-functional optical probe and potential removal system for arsenic (III) from water," *Journal of Hazardous Materials*, vol. 375, pp. 216–223, 2019.

[9] M. S. Najafinejad, P. Mohammadi, M. Mehdi Afsahi, and H. Sheibani, "Biosynthesis of Au nanoparticles supported on Fe_3O_4@polyaniline as a heterogeneous and reusable magnetic nanocatalyst for reduction of the azo dyes at ambient temperature," *Materials Science and Engineering: C*, vol. 98, pp. 19–29, 2019.

[10] S. Wei, W.-W. Wang, X.-P. Fu, S.-Q. Li, and C.-J. Jia, "The effect of reactants adsorption and products desorption for Au/TiO_2 in catalyzing CO oxidation," *Journal of Catalysis*, vol. 376, pp. 134–145, 2019.

[11] A. Kraus, K. Jainae, F. Unob, and N. Sukpirom, "Synthesis of MPTS-modified cobalt ferrite nanoparticles and their adsorption properties in relation to Au (III)," *Journal of Colloid and Interface Science*, vol. 338, no. 2, pp. 359–365, 2009.

[12] Z. H. Li, J. H. Bai, X. Zhang et al., "Facile synthesis of Au nanoparticle-coated Fe_3O_4 magnetic composite nanospheres and their application in SERS detection of malachite green," *Spectrochimica Acta Part A: Molecular and Biomolecular Spectroscopy*, vol. 241, p. 118532, 2020.

[13] D. T. Nguyen, T. Charinpanitkul, D. W. Park, and K. S. Kim, "Preparation of magnetite hollow structure for drug delivery application," *Journal of Nanoscience and Nanotechnology*, vol. 14, no. 10, pp. 7995–7999, 2014.

[14] D. T. Nguyen, D. W. Park, and K. S. Kim, "Seed-mediated synthesis of iron oxide and gold/iron oxide nanoparticles," *Journal of Nanoscience and Nanotechnology*, vol. 11, no. 8, pp. 7214–7217, 2011.

[15] S. Seino, T. Kusunose, T. Sekino et al., "Synthesis of gold/magnetic iron oxide composite nanoparticles for biomedical applications with good dispersibility," *Journal of Applied Physics*, vol. 99, no. 8, p. 08H101, 2006.

[16] J. Kudr, Y. Haddad, L. Richtera et al., "Magnetic nanoparticles: from design and synthesis to real world applications," *Nanomaterials*, vol. 7, no. 9, p. 243, 2017.

[17] M. A. M. Tarkistani, V. Komalla, and V. Kayser, "Recent advances in the use of iron–gold hybrid nanoparticles for biomedical applications," *Nanomaterials*, vol. 11, no. 5, p. 1227, 2021.

[18] S. Karamipour, M. S. Sadjadi, and N. Farhadyar, "Fabrication and spectroscopic studies of folic acid-conjugated Fe_3O_4@Au core-shell for targeted drug delivery application," *Spectrochimica Acta Part A: Molecular and Biomolecular Spectroscopy*, vol. 148, pp. 146–155, 2015.

[19] J. Li, Y. Hu, J. Yang et al., "Hyaluronic acid-modified Fe_3O_4@Au core/shell nanostars for multimodal imaging and photothermal therapy of tumors," *Biomaterials*, vol. 38, pp. 10–21, 2015.

[20] G. Zhou, Y. Wang, R. Zhou et al., "Synthesis of amino-functionalized bentonite/$CoFe_2O_4$@MnO_2 magnetic recoverable nanoparticles for aqueous Cd^{2+} removal," *Science of the Total Environment*, vol. 682, pp. 505–513, 2019.

[21] A. Virden, S. Wells, and K. O'Grady, "Physical and magnetic properties of highly anisotropic cobalt ferrite particles," *Journal of Magnetism and Magnetic Materials*, vol. 316, no. 2, pp. e768–e771, 2007.

[22] Z. Zi, Y. Sun, X. Zhu, Z. Yang, J. Dai, and W. Song, "Synthesis and magnetic properties of $CoFe_2O_4$ ferrite nanoparticles," *Journal of Magnetism and Magnetic Materials*, vol. 321, no. 9, pp. 1251–1255, 2009.

[23] M. Grigorova, H. J. Blythe, V. Blaskov et al., "Magnetic properties and Mössbauer spectra of nanosized $CoFe_2O_4$ powders," *Journal of Magnetism and Magnetic Materials*, vol. 183, no. 1-2, pp. 163–172, 1998.

[24] G. G. Zhanel, R. Wiebe, L. Dilay et al., "Comparative review of the carbapenems," *Drugs*, vol. 67, no. 7, pp. 1027–1052, 2007.

[25] C.-C. Sheu, Y.-T. Chang, S.-Y. Lin, Y.-H. Chen, and P.-R. Hsueh, "Infections caused by carbapenem-resistant enterobacteriaceae: an update on therapeutic options," *Frontiers in Microbiology*, vol. 10, 2019.

[26] J. Cielecka-Piontek, K. Michalska, P. Zalewski, and S. Zasada, "Comparative review of analytical techniques for determination of carbapenems," *Current Analytical Chemistry*, vol. 8, no. 1, pp. 91–115, 2012.

[27] C.-H. W. Chen Chun-Chi, K. Po-Yun, and Y.-L. Chen, "Nanomaterial-based adsorbents and optical sensors for illicit drug analysis," *Journal of Food and Drug Analysis*, vol. 28, no. 4, pp. 655–677, 2020.

[28] M. Shaban, M. Ibrahim, M. M-Ridha, and H. Hussein, "Adsorption of meropenem antibiotics from aqueous solutions on multi-walled carbon nanotube," *International Review of Civil Engineering*, vol. 11, no. 6, pp. 283–293, 2020.

[29] M. J. M-Ridha, Y. R. Hasan, and M. A. Ibrahim, "Adsorption kinetics and mechanisms for meropenem antibiotic removal in batch mode via rice husk functionalized with Mg/Fe-layered double hydroxides," *Separation Science and Technology*, vol. 56, pp. 2721–2733, 2020.

[30] Q. K. Nguyen, T. H. Hoang, X. T. Bui, T. A. H. Nguyen, T. D. Pham, and T. N. M. Pham, "Synthesis and application of polycation-stabilized gold nanoparticles as a highly sensitive sensor for molecular cysteine determination," *Microchemical Journal*, vol. 168, p. 106481, 2021.

[31] T. N. M. Pham, T. B. Le, D. D. Le et al., "Determination of carbapenem antibiotics using a purpose-made capillary electrophoresis instrument with contactless conductivity detection," *Journal of Pharmaceutical and Biomedical Analysis*, vol. 178, p. 112906, 2020.

[32] I. Langmuir, "The adsorption of gases on plane surfaces of glass, mica and platinum," *Journal of the American Chemical Society*, vol. 40, no. 9, pp. 1361–1403, 1918.

[33] E. E. Jasper, V. O. Ajibola, and J. C. Onwuka, "Nonlinear regression analysis of the sorption of crystal violet and methylene blue from aqueous solutions onto an agro-waste derived activated carbon," *Applied Water Science*, vol. 10, no. 6, 2020.

[34] A. M. Brown, "A step-by-step guide to non-linear regression analysis of experimental data using a Microsoft Excel spreadsheet," *Computer Methods and Programs in Biomedicine*, vol. 65, no. 3, pp. 191–200, 2001.

[35] H. Freundlich, "Über die Adsorption in lösungen," *Über Die Adsorption in Lösungen*, vol. 57U, no. 1, pp. 385–470, 1907.

[36] W. Khalid, F. Jafar, N. Iqbal et al., "Synthesis of gold-coated $CoFe_2O_4$ and their potential in magnetic hyperthermia," *Applied Physics A*, vol. 124, no. 7, p. 501, 2018.

[37] M. Muneeswaran, A. Akbari-Fakhrabadi, M. A. Gracia-Pinilla, J. C. Denardin, and N. V. Giridharan, "Realization of structural transformation for the enhancement of magnetic and magneto capacitance effect in $BiFeO_3$-$CoFe_2O_4$ ceramics for energy storage application," *Scientific Reports*, vol. 11, no. 1, p. 2265, 2021.

[38] J. Dong, P. L. Carpinone, G. Pyrgiotakis, P. Demokritou, and B. M. Moudgil, "Synthesis of precision gold nanoparticles using Turkevich method," *Kona Powder and Particle Journal*, vol. 37, pp. 224–232, 2020.

[39] J. Turkevich, P. C. Stevenson, and J. Hillier, "A study of the nucleation and growth processes in the synthesis of colloidal gold," *Discussions of the Faraday Society*, vol. 11, pp. 55–75, 1951.

[40] B. Stuart, *Infrared Spectroscopy: Fundamental and Applications*, John Wiley & Sons Ltd., 2004.

[41] P. K. Jain, K. S. Lee, I. H. El-Sayed, and M. A. El-Sayed, "Calculated absorption and scattering properties of gold nanoparticles of different size, shape, and composition: applications in biological imaging and biomedicine," *The Journal of Physical Chemistry B*, vol. 110, no. 14, pp. 7238–7248, 2006.

[42] S. Alekseeva, I. I. Nedrygailov, and C. Langhammer, "Single particle plasmonics for materials science and single particle catalysis," *ACS Photonics*, vol. 6, no. 6, pp. 1319–1330, 2019.

[43] A. O. Baskakov, A. Y. Solov'eva, Y. V. Ioni et al., "Magnetic and interface properties of the core-shell Fe_3O_4/Au nanocomposites," *Applied Surface Science*, vol. 422, pp. 638–644, 2017.

[44] M. R. Samarghandi, T. J. Al-Musawi, A. Mohseni-Bandpi, and M. Zarrabi, "Adsorption of cephalexin from aqueous solution using natural zeolite and zeolite coated with manganese oxide nanoparticles," *Journal of Molecular Liquids*, vol. 211, pp. 431–441, 2015.

[45] F. Kamar, A. Nechifor, G. Nechifor, T. Al-Musawi, and A. Mohammed, "Aqueous phase biosorption of Pb (II), Cu (II), and Cd (II) onto cabbage leaves powder," *International Journal of Chemical Reactor Engineering*, vol. 15, 2017.

[46] Y. Mao and Q. Yue, "Kinetic modeling of phosphate adsorption by preformed and in situ formed hydrous ferric oxides at circumneutral pH," *Scientific Reports*, vol. 6, no. 1, p. 35292, 2016.